Diffusion of oxygen vacancies formed at the anatase (101) surface:
An activation-relaxation technique study

Jeffrey Roshan De Lile [1,*] and Normand Mousseau[1,2,*]

[1]*Department of Physical Engineering, Polytechnique Montréal, Case postal 6079, Station Centre-Ville, Montréal, Québec, Canada H3C 3A7*
[2]*Succursale Centre-Ville, Département de Physique, Université de Montréal, Case Postale 6128, Montréal, Québec, Canada H3C 3J7*

TiO_2 is a technologically important material. In particular, its anatase polymorph plays a major role in photocatalysis, which can also accommodate charged and neutral vacancies. There is, however, scant theoretical work on the vacancy charge and associated diffusion from surface to subsurface and bulk in the literature. Here, we aim to understand $+2$ charge and neutral vacancy diffusion on anatase (101) surface using 72- and 216-atom surface slabs employing a semilocal density functional and the Hubbard model. The activation-relaxation technique nouveau coupled with QUANTUM ESPRESSO is used to investigate the activated mechanisms responsible for the diffusion of oxygen vacancies. The small-slab model overstabilizes the $+2$ charged topmost surface vacancy, which is attributed to the strong Coulomb repulsion between vacancy and neighboring Ti^{+4} ions. The larger slab allows atoms to relax parallel to the surface, decreasing the $+2$ charged topmost surface vacancy stability. The calculated surface-to-subsurface barriers for the $+2$ charged vacancy and diffusion of the neutral vacancy on a slab of 216 atoms are 0.82 and 0.52 eV, respectively. Furthermore, the bulk vacancy prefers to migrate toward the subsurface with relatively low activation barriers 0.19 and 0.27 eV and the reverse process has to overcome 0.38- and 0.40-eV barriers for the $+2$ charged and the neutral vacancies. This explains the experimentally observed high concentration of vacancies at the subsurface sites rather than in the bulk, and the dynamic diffusion of vacancies from the bulk to the subsurface and from the subsurface to the bulk is highly likely on the surface of anatase (101). Finally, we provide a plausible explanation for the origin of recently observed subsurface-to-surface diffusion of oxygen vacancy from the calculated results.

I. INTRODUCTION

Titanium dioxide, TiO_2, is one of the most stable, versatile, low-cost, high natural abundance, and nontoxic materials. Its rich set of properties has made it widely used as an efficient photocatalyst, pollutant degradation, antibacterial agent, hydrogen evolution, water splitting, and CO_2 reduction. TiO_2 naturally occurs as many polymorphs, including anatase, rutile, and brookite. Among those polymorphs, rutile is the most stable form under ambient conditions. However, there is a consensus among material scientists that anatase is the most active polymorph of TiO_2 for photocatalysis [1]. This has led anatase to be investigated extensively, both experimentally and theoretically, using various methods, including spectroscopic methods (x-ray photoelectron spectroscopy, XPS) [2], UV-vis absorption [3], angle-resolved photoemission spectroscopy [4], EPR [5]), and density-functional theory (DFT) [6], in order to understand the electronic structure and optical properties.

TiO_2 wide band gap curtails the photocatalytic activity in the visible light and infrared regions. Hence doping, defect formation, and surface modifications are employed to improve the visible light absorption. Cation doping sites can act as recombination centers for photogenerated charge carriers, decreasing their potential to support surface redox reaction [1]. Anion doping, on the other hand, is expected to improve visible light adsorption [7]. Some researchers proposed that nitrogen (N) doping of TiO_2 could increase the photoactivity in the visible light region through the narrowing of the band gap [8]. However, a significant reduction of the band gap may lead to a material's chemical composition change that can be accompanied by structural and electronic properties change as well [9]. A recent study by Foo and co-workers found a cubic titanium oxynitride phase formation in highly nitrogen-doped anatase that provides evidence for such a chemical composition change [10]. However, the presence of oxygen vacancies is also correlated with the enhanced visible light photoactivity of doped TiO_2 [11]. Thus, researchers have turned their focus towards oxygen vacancies: in some cases, these produce a narrow band of defect-derived states experimentally observed at about 0.9 eV below the conduction-band edge in agreement with ultraviolet photoemission spectroscopy and electron energy-loss spectroscopy studies [12–14]. In addition, XPS and conductivity measurements at the defective surfaces show formation of Ti^{+3} ions and reduction of conductivity also evidence the localized nature of the excess electrons [2,15,16]. Among these vacancy states, the bridging oxygen vacancy formation has been largely supported by spectroscopic and chemical evidence on TiO_2 samples sputtered and annealed in ultrahigh vacuum [17]. Moreover,

---

*Corresponding authors: jeffrey.delile@polymtl.ca, normand.mousseau@umontreal.ca

comparative studies of anatase and rutile show anatase surfaces have a lower tendency to release lattice oxygen atoms whereas rutile surfaces form a large amount of oxygen defects [18,19].

Among all surfaces, anatase (101) is most widely investigated due to its superior stability and higher photocatalytic ability. Cheng and Selloni provided the first theoretical evidence for the subsurface diffusion of a neutral surface vacancy with a 0.74-eV barrier [20]. Scheiber *et al.* confirmed that theoretical prediction using electron bombardment experiment of anatase (101) surfaces [17]. Scheiber and co-workers assumed an activation energy barrier ranging from 0.6 to 1.2 eV for subsurface diffusion and the authors argued that such a range is not unreasonable as the vacancy diffusion barrier depends on the immediate environment of each vacancy. The metastable surface neutral oxygen vacancy formation involves dissociation of shorter bonds of Ti–O at the anatase (101) surface creating one fivefold, and one highly unstable fourfold-coordinated Ti^{+3} cation [20]. Conversely, removal of an oxygen atom from the subsurface creates only stable fivefold-coordinated Ti^{+3} cations. Thus, the subsurface vacancies are more stable than those at the (101) surface. However, Setvin *et al.* demonstrated for the first time that the relative stability of subsurface and surface vacancies on anatase (101) could be reversed by adsorbing an oxygen molecule on the surface and by applying an electric field under experimental conditions [21]. The authors elucidated the migration of the bulk oxygen vacancy to the surface, and showed that the vacancy interacts with the adsorbed oxygen species. Recent theoretical investigations of water (H_2O) and hydrogen sulfide (H_2S) adsorption on the anatase (101) surface also observe similar changes of the relative stability and demonstrate subsurface vacancy diffusion towards the surface to interact with the adsorbate species [22,23]. Moreover, electric-field induced subsurface vacancy migration towards the surface suggests vacancy charge might be responsible for such stability change in addition to the surface relaxations. These studies demonstrate the complex nature of anatase (101) surface. Yet, so far, there is no consensus among researchers regarding the bulk vacancy stability with respect to the subsurface vacancy. Cheng and Selloni reported a 3.69-eV (generalized gradient approximation–Perdew-Burke-Ernzerhof (GGA-PBE) neutral vacancy formation energy in the bulk, which is very similar to their reported value of subsurface vacancy formation energy using 216-atom slab with six layers [19,20]. The authors also computed bulk diffusion barrier using anatase bulk unit cell and found ∼0.17-eV activation barrier. However, no information was presented about bulk-to-subsurface vacancy migration on 216 atoms slab. Deak and co-workers calculated neutral vacancy formation energy on bulk using 72-atom slab with three layers [24]. The reported bulk formation energy is 5.35 eV Heyd-Scuseria-Ernzerhof hybrid functional 06 (HSE06), substantially larger than their subsurface and surface neutral vacancy formation energies. Li *et al.* also reported bulk vacancy formation energy for neutral vacancy on anatase 144-atom slab with four layers [25]. The calculated bulk vacancy formation energies of 4.27 eV (GGA-PBE) and 4.95-eV (modified screened-exchange hybrid local density approximation) were found to be larger than subsurface vacancy formation energies, but smaller than the topmost

surface vacancy formation energies. Thus, our understanding of vacancy formation and diffusion on anatase (101) is far from complete.

The wide range of surface-to-subsurface diffusion barriers, inconsistencies of the results for bulk vacancy stability, and lack of diffusion barriers associated with both +2 charged and neutral vacancies warrant this investigation on the anatase (101) surface. Despite a number of studies related to electronic structure, vacancy formation energy, and defect states in the bulk and surfaces of anatase, a few have focused on the link between the oxygen vacancy charge and its diffusion from surface to subsurface and subsurface to bulk. Therefore, in this work, we investigate the influence of vacancy charge on the stability of vacancies using neutral and +2 charged vacancies on the anatase surface, subsurface, and bulk *in silico* using 72- and 216-atom surface supercells. Semilocal density functional and the Hubbard model are employed to understand the vacancy formation energies and the activation-relaxation technique nouveau (ARTn) in its recent implementation with QUANTUM ESPRESSO software suite is used to elucidate activation mechanisms responsible for +2 charged and neutral oxygen vacancy diffusion [26].

The outline of the paper is as follows. First, we describe the computational details for oxygen vacancy formation energy and diffusion barrier calculations in Sec. II; then, we focus on result and discussion in Sec. III with a brief comparison of semilocal functional (GGA-PBE) results with Hubbard model (DFT+U). Section III consists of two subsections where we describe the results obtain from 216-atoms large-slab model for surface vacancy diffusion to subsurface in Sec. III A. Then we turn our attention into bulk vacancy diffusion to subsurface in Sec. III B. Finally, we summarize the import findings as conclusions in Sec. IV.

II. COMPUTATIONAL DETAILS

In TiO_2 each Ti atom donates four electrons to two oxygen atoms, resulting in Ti^{+4} and O^{2-} nominal charges. Upon the loss of an O atom in a TiO_2, the electron pair originally trapped by the oxygen are donated to the lattice and remain trapped in a cavity of oxygen vacancy (V_O) that gives rise to a color center [1]. These electrons are commonly named excess electrons in the literature [16]. A neutral color center is equivalent to a pair of electrons associated with the V_O. For the sake of simplicity, a neutral color center is referred to as a neutral vacancy throughout the paper; electrons left in the vacancy interact with adjacent Ti^{+4} ions to give Ti^{+3} centers while an electron pair-deficient oxygen vacancy is referred to as a doubly charged color center [1]. In this paper, a doubly charged color center is named as a +2 charged vacancy to minimize technological jargon. In addition, 72-atom and 216-atom slabs are referred to both nondefective and defective slabs unless otherwise specified.

Initial structural relaxation of the anatase (101) surfaces and bulk structures is performed using spin-polarized GGA-PBE exchange-correlation functional within plane-wave pseudopotential scheme implemented in QUANTUM ESPRESSO (QE) software suite [27,28]. The neutral and the +2 charged states of the oxygen vacancies (denoted V_O^0 and V_O^{+2}) are used as the intrinsic defects. A model structure with three O-Ti-O layers

is used to simulate the TiO_2 (101) stoichiometric surface with (1×2) supercell of 72 atoms ($Ti_{24}O_{48}$). The supercells are further tested for a 2×2×1 k-point mesh but the difference in formation energies of defects is found to be negligible with respect to gamma-point calculations. Thus, all the vacancy formation energies reported here are obtained from gamma-point only calculations. A vacuum layer of 12 Å is used to separate the periodic images along the z axis direction for all the slab models. The interaction between core and valence electrons is described by ultrasoft pseudopotentials and a kinetic energy cutoff of 50 Ry for smooth part of the wave functions is used [29]; $2s^2\,sp^4$ and $3s^2\,3p^6\,3d^2\,4s^2$ are treated as the valence electrons of oxygen and titanium, respectively. The computed bulk lattice parameters $a = 3.78$ Å and $c = 9.45$ Å (experimental values: $a = 3.77$ Å and $c = 9.50$ Å [30]) are obtained by relaxing a tetragonal bulk unit cell. A 5×5×2 k-point mesh is used to sample the corresponding Brillouin zone for the four TiO_2 units containing bulk unit cell. In addition to the 72-atom surface supercells, 216-atom ($Ti_{72}O_{144}$) four O-Ti-O layers with (2×3) large surface supercells are employed for anatase (101) surface studies. A bulk oxygen vacancy is also computed using a 3×3×2 supercell with 216 atoms. As with the 72-atom system, k-point sampling is limited to the gamma point for 216-atom surface slabs and bulk supercells. We perform test calculations on 72-atom anatase (101) surface supercells and find that the two unpaired electrons associated with the Ti^{+3} in neutral oxygen vacancy can be represented as singlet and triplet states that are degenerate at the GGA level using PBE exchange-correlation functional [31]. However, standard DFT functionals tend to delocalize electrons over the crystal, particularly for the material that contain transition elements with partially filled d or f electronic orbitals; thus, Hubbard-like correction term (U) is applied to d orbitals of Ti in anatase [32,33]. The DFT+U calculations are performed on both 72- and 216-atom-TiO_2(101) slabs using gamma point with the PBE functional and spin-polarized scheme. After extensive testing of the Hubbard U parameter using 72-atom slab, $U = 2$ eV is selected for the optimizations and diffusion barriers calculations due to destabilization of subsurface vacancy beyond this value for the neutral oxygen vacancies on the anatase (101) surface. This is graphically illustrated in Fig. S1 of the Supplemental Material [34]. During the structural optimizations, all the atoms of the slab are allowed to move except those in the bottom layer. The Broyden-Fletcher-Goldfarb-Shanno algorithm is employed for all the ionic steps during the optimization with the fixed occupations due to semiconducting nature of this material [35]. For density of states (DOS) and projected density of states (PDOS) calculations 8×8×1 larger k-point mesh is used for both DFT and DFT+U. Procedure documented in the QUANTUM ESPRESSO user guide is followed starting from the preoptimized defective 72-atom anatase (101) surface structure for the computation of PDOS and DOS.

Neutral oxygen vacancies (V_O) in anatase (101) surface are simulated by removing one oxygen atom from both 72- and 216-atom supercells. A charged vacancy (V_O^{+2}) is created by removing one oxygen atom and two electrons from the supercells (homogeneous background charge is added to compensate for extra charges to remove electrostatic divergence if the periodic cell is not neutral) [36]. To determine the relative

stability of neutral and +2 charged states, the formation energies (E_{form}) of V_O and V_O^{+2} defects are computed assuming thermodynamic equilibrium with a reservoir of oxygen (oxygen chemical potential μ_O). The oxygen chemical potential is conveniently referred to the energy E_{tot} of an O atom in O_2, which is equivalent to $1/2E_{tot}(O_2) + \mu_O'$. In this work, $\mu_O' = 0$ is assumed, which corresponds to the O-rich limit at which oxygen condensation occurs. Therefore, formation energy is defined as follows [15]:

$$E_{form}\left(V_O^q\right) = E_{def}^q - E_{no-def} + {}^1/_2\, E_{tot}(O_2) + \mu_O' + q(E_V + E_F), \tag{1}$$

where q is charge state of the oxygen vacancy, E_{def}^q and E_{no-def} are total DFT/DFT+U energy of the defect-containing supercell with vacancy charge q and pristine supercell without the defect, respectively. E_F and E_V are the Fermi energy of the material which is the chemical potential of the electron reservoir and the energy of the valence-band maximum, respectively. Madelung corrections for the electrostatic interaction between homogeneous background charge and the charge defect are not calculated in the present work since the dielectric constant of the TiO_2, in particular, the ionic contributions are fairly large [15].

All structures are optimized before proceeding with diffusion-barrier calculations. Diffusion pathways and barriers are calculated for both the GGA-PBE and the DFT+U levels for 72-atom supercells. However, GGA-PBE and DFT+U are tested and used only for a few activation barrier computations on 216-atom slabs. Here, the activation-relaxation technique nouveau coupled to the QE code is utilized to compute the activation energies and diffusion pathways [26,37–39]. Unlike string methods such as nudged elastic band, that require saddle-point and final-state configurations of the material as initial guess structures in addition to the initial state, ARTn requires only initial minimum-energy configuration of the material to search the minimum-energy pathway (MEP) and associated activation barriers. Therefore, prior knowledge of the complex reaction pathways and of their structural configurations is not needed to apply ARTn method. In the implementation of ARTn, which is referred to as *ab initio*-ARTn, the DFT-based energy and force engine of the QE is used for energy and force evaluation [26]. In this work, fully relaxed initial configuration of the vacancy structure is used to initiate the MEP search and the user selects the direction of the oxygen atom along which the atom and its neighboring environment is pushed iteratively based on the vacancy location to reduce the computational time.

ARTn events are generated as follows: the target oxygen atom is moved in a user-defined direction iteratively. At each step, a minimum relaxation is performed in the perpendicular hyperplane to prevent collision and allow the whole system to react to this displacement. Before a new step, the local curvature is computed using a Lanczos algorithm in order to extract the lowest eigenvalue and its corresponding eigenvector and this step is repeated, with a small push in the defined direction, as long as the lowest eigenvalue is above a given threshold (set here to 0.03 eV/Å) [40]. Once the system leaves the initial harmonic basin, as signaled with a negative eigenvalue, the system is then pushed along the associated
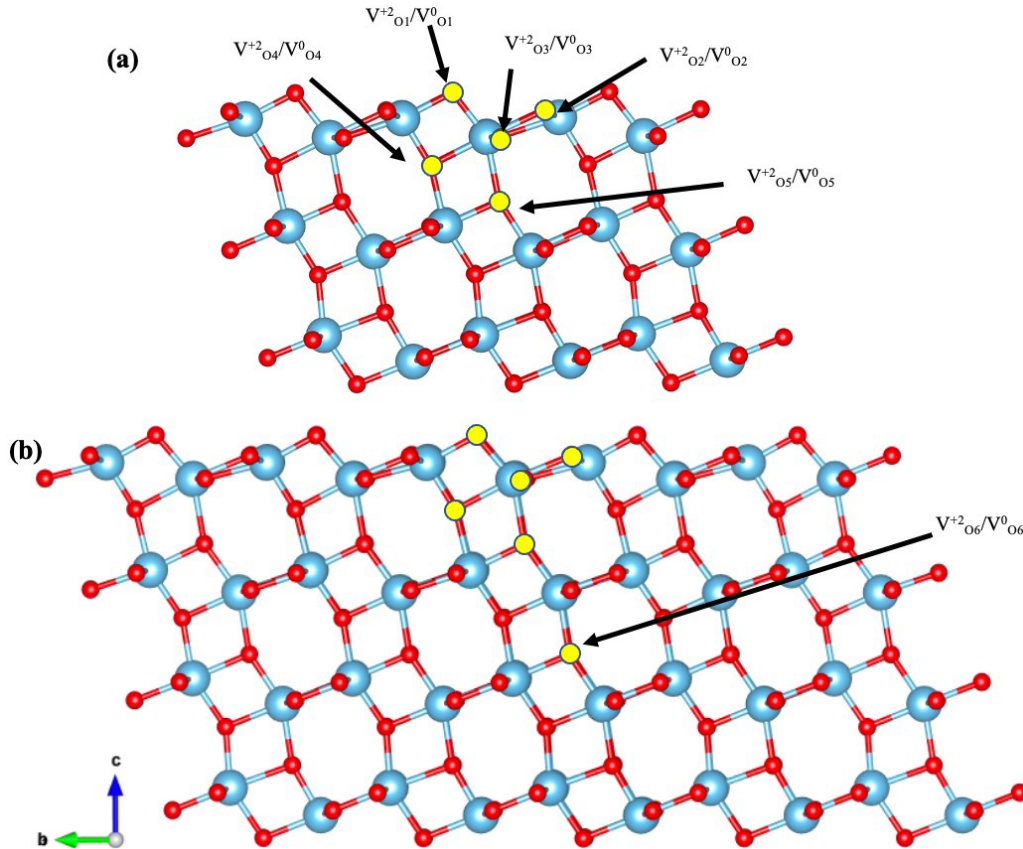
FIG. 1. Side view of the anatase (101) surface supercell of 72 atoms (a) and 216 atoms (b). Oxygen vacancy positions are labeled for easy references. The larger 216-atom slab is used to compute bulk vacancy formation energy as well, which is denoted as V_{O6}^0 for neutral vacancy and V_{O6}^{+2} for +2 charged vacancy. Vacancies are presented as yellow dots, oxygen red, and titanium blue.

direction of negative curvature, while minimizing in the perpendicular direction. No constraint is placed, at this point, on the moving atoms which are iteratively pushed in the user-defined direction, while a minimal relaxation is performed in the perpendicular hyperplane, until being out of its harmonic basin. This movement induces local deformation around the selected oxygen atom and its nearest neighbors. Then, the lowest eigenvalue of the Hessian matrix is calculated using Lanczos algorithm [40]. This continues until the lowest eigenvalue falls below a threshold value, which indicates the system has left the harmonic basin and moved beyond the inflection line. Then, the activation part of ARTn begins to push from the inflection to the saddle point following the direction defined by the eigenvector corresponding to the lowest eigenvalue. After each push along the oxygen-atom movement direction, the whole system is relaxed in the hyperplane perpendicular to the above direction. This iterative procedure, including the calculation of the curvature, is repeated until the total force falls below a given threshold defining the saddle point. Here, 0.03 eV/Å is used as a threshold value for total force to define convergence at the saddle point. From the saddle point, the configuration is further pushed along the eigenvector both away from the initial minimum and towards it. The two configurations obtained from the two pushes are then fully relaxed and compared with the initial minimum. The latter step ensures that the saddle point is directly connected to the initial minimum without an intermediate state(s). Thus, it confirms

the fully connected event from initial state to saddle point and to final state. Interested readers are directed to Ref. [26] for details of the method.

III. RESULTS AND DISCUSSION

Comparing GGA-PBE optimized 216-atom and 72-atom anatase (101) surface structures with the recently elucidated experimental bond lengths of the anatase surface (see Fig. S2 for atom numbering scheme and Table S1 in the Supplemental Material [34]), we find that our theoretically predicted surface structures match well with the experimental bond lengths [41]. The maximum difference between the experimental and the theoretically predicted bond lengths of the 72-atom slab surface is 0.16 Å and that is of the 216-atom slab is 0.23 Å; overall, the theoretical structures display slightly elongated bonds. We attribute the 0.23-Å difference in the larger four-layer slab model to stronger structural relaxation compared to the three-layer 72-atom slab. A side view of the 72-atom and 216-atom supercells with the vacancy numbering scheme is depicted in Fig. 1, and the vacancy formation energies of the neutral vacancies computed from the GGA-PBE level of theory are listed in Table I. The vacancy numbering scheme in Fig. 1 shows the vacancy numbers as a subscript depending on their relative height as measured from the surface while the vacancy charge is represented as a superscript. For example, topmost neutral surface oxygen vacancy is

TABLE I. Formation energies E_{form} of neutral defects at different surface and subsurface sites for an anatase (101) slab of 72 atoms and 216 atoms calculated at the GGA-PBE level for oxygen-rich conditions. Our results are compared with the literature reported values. Here, V_{O6}^0 represents the bulk neutral oxygen vacancy formation energy computed from the 216-atom slab model.

Defect site	72 atoms E_{form} (eV)	72 atoms E_{form} (eV)	96 atoms E_{form} (eV)	144 atoms E_{form} (eV)	144 atoms E_{form} (eV)	216 atoms E_{form} (eV)	216 atoms E_{form} (eV)
V_{O1}^0	4.24	4.39	–	4.18	5.07	4.01	4.15
V_{O2}^0	5.51	5.43	–	4.89	5.56	5.00	–
V_{O3}^0	5.07	4.95	–	4.54	5.35	4.37	–
V_{O4}^0	4.61	–	–	–	–	–	–
V_{O5}^0	4.04	4.18	5.12	4.00	4.91	3.71	3.69
V_{O6}^0	–	–	–	–	–	3.83	–
Bulk	–	–	–	–	–	3.79	3.69
	This work	Ref. [20]	Ref. [43]	Ref. [22]	Ref. [23]	This work	Ref. [20]

denoted as V_{O1}^0, and the deepest subsurface neutral oxygen vacancy in the 72-atom slab of the anatase (101) surface is denoted as V_{O5}^0. The small-slab model is computationally less demanding and widely used in literature [19,20,24,42]. Thus, the 72-atom slab is initially used to explore formation energies and activation energy barriers of oxygen vacancies on anatase (101) surface with inequivalent oxygen vacancy sites.

The vacancy formation energy of the subsurface layer vacancy V_{O5}^0 is the lowest among all the considered neutral vacancies on the anatase (101) surface. In the 72-atom slab, the topmost surface vacancy V_{O1}^0 is ∼0.2 eV higher in energy than V_{O5}^0, quantitatively consistent with the previous theoretical studies of 72-atom and 144-atom slabs [19,20,22,23]. The V_{O4}^0 vacancy is considered very unstable in previous studies; however, we find that this vacancy is metastable as it has to overcome activation energy barrier for diffusion. The 216-atom slab shows ∼0.3-eV energy difference between the topmost surface and the subsurface oxygen vacancy formation energy. The bulk neutral vacancy stability V_{O6}^0 stands between the topmost surface vacancy and the subsurface vacancy. The bulk neutral vacancy formation energy is computed using 216-atom bulk supercell and agrees well with its evaluation in the 216-atom surface slab. Deak *et al.* recently computed the vacancy formation energy for the topmost layer, the subsurface, and the bulk of 72-atom supercell with HSE06 hybrid functional and found that the bulk vacancy formation energy is the highest among all [24]. Li *et al.* also reported surface, subsurface, and bulk vacancy formation energies from GGA and screened hybrid functional [25]. The authors show that the bulk vacancy formation energy is higher than the subsurface, but lower than the topmost surface from both methods. Thus, our bulk vacancy formation energy is also in agreement with Li and co-workers. Table S2 [34] shows the vacancy formation energies for +2 charged vacancies, which are given at the higher Fermi-energy level on the conduction band minimum (CBM) in oxygen-rich conditions. Note that the V_{O5}^{+2} subsurface vacancy is 0.06 eV higher in energy than the V_{O1}^{+2}. Therefore, the +2 charged topmost layer vacancy on the anatase (101) surface is slightly more stable than the subsurface V_{O5}^{+2} on the 72- atom slab. In addition, the V_{O4}^{+2}

vacancy is not observed as the V_{O4}^{+2} vacancy diffuses to the V_{O1}^{+2} vacancy site during the structural optimization, along a barrierless trajectory. On the contrary, a larger 216-atom slab shows a subsurface vacancy 0.19 eV more stable than that of the topmost surface vacancy. Computed bulk vacancy formation energy of the V_{O6}^{+2} is quantitatively identical to the topmost surface vacancy formation energy. The bulk +2 charged vacancy formation energy computed from 216-atom bulk supercell is also comparable with the V_{O6}^{+2} bulk vacancy formation energy. Generally, V_{O2}^0, V_{O3}^0, V_{O2}^{+2}, and V_{O3}^{+2} vacancies have significantly higher vacancy formation energies than V_{O1}^0, V_5^0, V_{O1}^{+2}, and V_{O5}^{+2}.

Semilocal functionals such as PBE tend to delocalize electrons [6]. Therefore, the DFT+U method is applied to all the above vacancies in both neutral and +2 charged states and is tested for the most suitable Hubbard parameter value using 72-atom slab. Starting from the GGA-PBE optimized anatase (101) surface structures, a range of Hubbard values from 1 to 7 eV is applied. For neutral vacancies, above 2 eV and higher Hubbard parameter stabilizes the surface V_{O1}^0 vacancy; thus, stability crossover from subsurface-to-surface oxygen vacancy is observed. Nevertheless, according to the theoretical, and experimental observations, neutral subsurface oxygen vacancy V_{O5}^0 should be more stable; consequently, the top-layer surface oxygen vacancy should diffuse to the subsurface [17,20]. As a result, 2-eV Hubbard parameter value is chosen for the DFT+U calculations. The applied Hubbard values do not show such a stability crossover effect in the +2 charged vacancies. This can be attributed to the higher stability of V_{O1}^{+2} on the topmost surface layer of the 72-atom supercell, as illustrated in Fig. S1 [34]. The applied Hubbard value-induced crossover in relative stabilities of V_{O5}^0 to V_{O1}^0 is observed by Cheng *et al.* who predicted that $U = 3$ eV is the best value for the anatase (101) surface studies [20]. However, we find that a 3-eV on-site Hubbard value affects profoundly the stability of the topmost surface neutral vacancies.

The PDOS is calculated from the DFT+U ($U = 2$ eV). Although this Hubbard value underestimates the band gap of the anatase (101) surfaces consisting of the neutral and the +2 charged oxygen vacancies, electron localization at the midgap

states are observed for the neutral-charge oxygen vacancy (see Fig. S3 in Supplemental Material [34]). Therefore, a 2-eV Hubbard parameter is still sufficient to localize electrons at vacancy site on the anatase (101) surface. The localization of electrons occurs at 0.48 and 0.46 eV below CBM for the V_{O5}^0 vacancy. These values are comparable with the literature [20]. Although the 2-eV Hubbard parameter satisfies the electron localization, the defect states in the band gap occur closer to the CBM. Applying higher Hubbard values such as 3 and 3.5 eV move the gap states deeper into the band gap 0.55, 0.59, and 0.86, and 0.91 eV, respectively. However, we cannot use such high-U values of the Hubbard parameter as they significantly affect the stability order of the vacancies (Fig. S1 [34]). The selected 2-eV Hubbard U value does not alter the defect formation energies considerably since the anatase valence band is completely filled. Therefore, these excited electronic states at the band gap cannot fall back into the valence band. Moreover, electrons are in localized states sufficiently below the CBM so that it is unlikely that they will diffuse into the conduction band as well. Figure S4 [34] provides vacancy formation energies for all the +2 charged and neutral vacancies in 72-atoms (FIG. S4 (a)) and 216-atoms supercells (FIG. S4 (b)) of the anatase (101) surfaces computed with DFT+U at a U value of 2 eV. As can be seen, +2 charged vacancy formation is favorable at all the Fermi levels. Figure S4(a) [34] clearly shows higher stability of V_{O1}^{+2} vacancy site on the smaller 72-atom slab. Therefore, both GGA-PBE and DFT+U methods predict higher stability on the top-layer surface +2 charged vacancy on the 72-atom slab. This implies the 72-atom slab is not adequate to represent +2 charged anatase (101) surface vacancy. The larger 216-atom slab allows to relax atoms parallel to the surface which reduces the +2 charged topmost surface vacancy stability and leads to V_{O5}^{+2} subsurface vacancy becoming the most stable vacancy site. Since all the other vacancy formation energies and diffusion barriers computed on smaller slab agree well with the larger-slab model, the 216-atom is primarily used for the discussion. We note also that the bulk vacancy formation energies computed on a 216-atom bulk supercell and a 216-atom surface slabs (V_{O6}^{+2}/V_{O6}^0) are higher than the topmost surface and the subsurface vacancy formation energies. Thus, the DFT+U computed bulk vacancy formation energies deviate from the GGA-PBE results. However, a hybrid functional study with HSE06 shows similar trend comparable with our DFT+U result [24]. This suggests the vacancy formation energy is very sensitive to the computational method and functionals.

Although extra charge distribution in 3D structures is very well compensated by the "Jellium" background charge to keep the total charge of the system neutral, spurious charge states interacting with the Jellium can cause an error in the absolute value of defect formation energy for charged defects, in particular, low-dimensional systems and supercell slab models with a vacuum [44,45]. Such shortcomings can affect the validity of the comparison of the +2 charged vacancy formation energy with the neutral vacancy formation energy. Comparing relative vacancy formation energies with respect to the subsurface vacancy formation energy based on the total energy of each defect structure, we find relative stability order and the magnitude of the energy difference between each vacancy for both vacancy types. The errors in the vacancy formation

energies due to the compensating background charge interaction with the charged defect cancel out in such an analysis (not shown). Moreover, a recent study concluded the anatase (101) surface charge vacancy formation energy depends on the choice of the vacuum spacing as well [46]. As we do not apply a correction scheme, the $12 - \text{Å}$ vacuum spacing used in this work may overestimate the 2+ charged vacancy formation energy by 0.2 eV. However, the 2+ charge state is more favorable at all Fermi levels is not sensitive to an error of this size. Furthermore, our vacancy formation energies agree well with the previous studies [20,25]. Therefore, our charged vacancy formation energies can be compared with the neutral vacancy formation energies.

A. Surface and subsurface diffusion pathways

The diffusion barriers computed with the GGA-PBE method are presented in Table II for 72-atom smaller slab and in Table III for 216-atom larger slab. In order to keep the calculations consistent, mechanisms are described from the higher-energy vacancy position to the lower-energy vacancy position migration throughout the paper, except for the surface-to-subsurface diffusion on 216-atom slab. All the GGA-PBE level calculated potential-energy profiles and mechanisms for the 72-atom supercells with single point defect are illustrated from Figs. S5 to S9 in Supplemental Material [34]. Corresponding calculations from the DFT+U level are illustrated in Figs. S10(a) to S10(h), and activation energy barriers are also tabulated in Tables S3 and S4 for the small and the large supercells, respectively [34]. Remarkable similarity in the potential-energy profiles and the vacancy migration barriers computed from semilocal functional and Hubbard model suggests that, in spite of its aforementioned limitations, GGA-PBE level computations are sufficient to accurately predict diffusion barriers and corresponding vacancy migration mechanisms. However, we note that V_{O1}^0 to V_{O5}^0 surface-to-subsurface diffusion barriers computed from the DFT+U method for both smaller and larger slab models are significantly smaller than the GGA-PBE level computed values. That may be attributed to the strong localization of two electrons (polaron formation) at the neighboring Ti^{+3} ions surrounding the topmost surface vacancy site [24]. Structural deformation associated with the electron localization at the vacancy site may lower the activation barrier. Nevertheless, this is beyond the scope of the present work as our primary objective is to establish the vacancy diffusion directions on the anatase (101) surface and the barriers associated with the +2 charged and the neutral vacancies.

Here, first we focus on surface-to-subsurface diffusion barriers and pathways on +2 charged and neutral oxygen vacancies. The neutral and the +2 charged vacancies diffusion from the surface to the subsurface show the expected behavior on 216-atom slabs. The neutral vacancy diffusion barrier 0.52 eV is relatively lower than that of the +2 charged vacancy 0.82 eV for the large supercell, respectively. Figure 2 illustrates subsurface-to-surface diffusion pathway and potential-energy profile associated with 216-atom slab calculation. Here, the subsurface most stable vacancy site migration to the topmost surface is computed in order to compare with 72-atom slab neutral vacancy calculation. All the

TABLE II. Diffusion barriers (E^A) of neutral and +2 charged defects on the different surface and subsurface sites of an anatase (101) slab of 72 atoms calculated at the GGA-PBE level using ARTn coupled to QE.

Pathway	E^A neutral vacancy direct pathway (eV)	E^A neutral vacancy inverse pathway (eV)	E^A + 2 charged vacancy direct pathway (eV)	E^A + 2 charged vacancy inverse pathway (eV)	Ref. [20] (eV) Direct pathway	Ref. [20] (eV) Inverse pathway
$V_{O1} \rightarrow V_{O5}$	0.60	0.82	0.76	0.72	0.74	0.95
$V_{O1} \rightarrow V_{O3}$	1.44	0.59	1.42	0.31	1.34	0.78
$V_{O1} \rightarrow V_{O2}$	3.00	1.73	3.45	1.70	1.52	0.47
$V_{O2} \rightarrow V_{O3}$	0.11	0.54	0.03	0.66	0.30	0.78
$V_{O3} \rightarrow V_{O5}$	0.71	1.76	0.64	1.70	0.78	1.59

computed subsurface-to-topmost surface diffusion involves two steps; first the subsurface (or surface) vacancy migrates to the V_{O4}^{+2}/V_{O4}^{0} site; then, the vacancy escapes from this unstable state and diffuses to the final surface (subsurface) vacancy site. During this process two oxygen atoms are displaced substantially, which are colored in black for easy visualization and the vacancy site is represented as a yellow circle. The potential-energy profiles represent the relative stability of the vacancy states and the activation barrier. In addition to this mechanism, V_{O3}^{+2}/V_{O3}^{0} surface vacancies can migrate to V_{O5}^{+2}/V_{O5}^{0} sites. Larger 216-atom slab calculation reveals activation energy barriers 0.73 and 0.67 eV for the +2 charged and the neutral vacancies, respectively. These calculated values for surface-to-subsurface vacancy diffusions are consistent with the theoretical result and experimental range of 0.6 to 1.2 eV

further convince GGA-PBE level of theory is sufficient for the activation barrier calculations [17,20].

In order to completely describe vacancy migration processes on the anatase (101) surface, we also compute surface vacancy diffusion. The larger 216-atom slab calculation confirms the metastable nature of V_{O2}^{+2}/V_{O2}^{0} vacancies, which is observed for smaller slab model. In fact, DFT+U level calculations show barrierless vacancy diffusion from V_{O2}^{+2} towards V_{O3}^{+2}; hence, we do not take V_{O2}^{+2}/V_{O2}^{0} vacancies into account for activation-energy barrier calculations on the larger slab models. Instead, we focus on V_{O3}^{+2}/V_{O3}^{0} vacancies migration to V_{O1}^{+2}/V_{O1}^{0}. The energy barrier for +2 charged V_{O3}^{+2} vacancy site diffusion towards V_{O1}^{+2} is 0.73 eV and for the similar diffusion pathway for the corresponding neutral vacancy is 0.78 eV. Overall, anatase (101) surface neutral vacancy migration
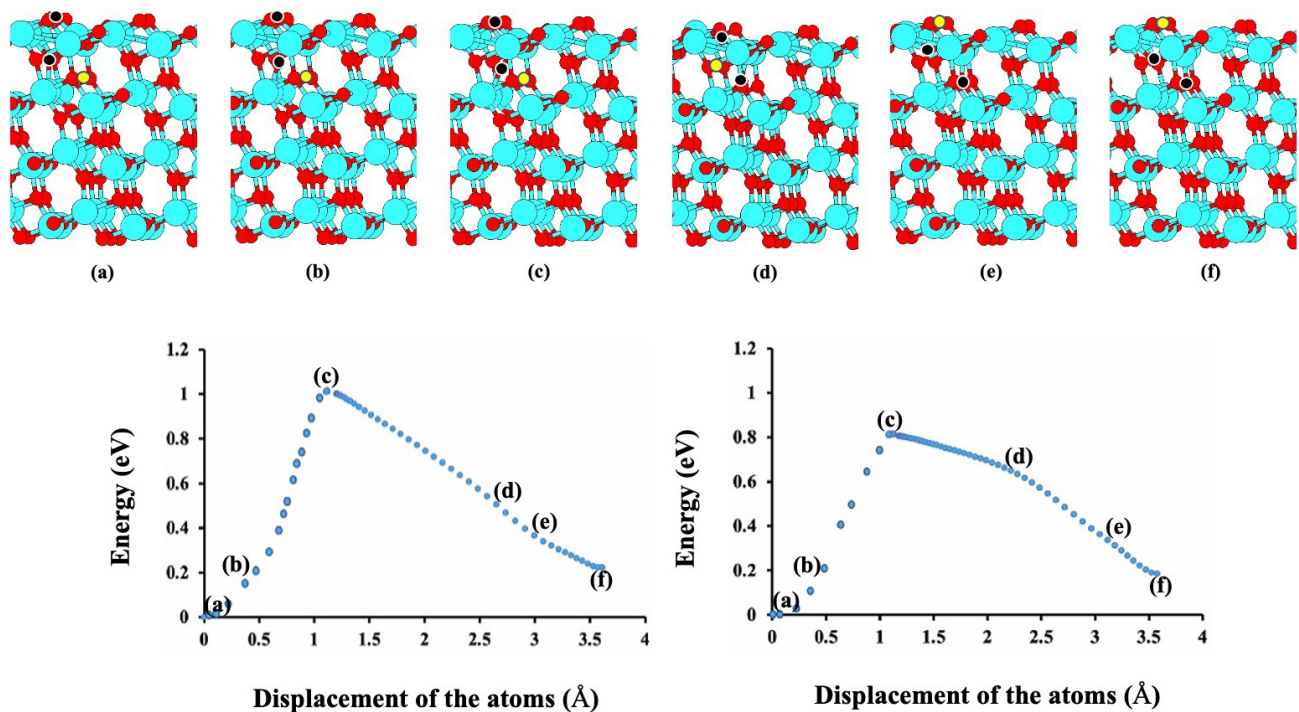

FIG. 2. Potential-energy profile along $V_{O5}^{+2}/V_{O5}^{0} \rightarrow V_{O1}^{+2}/V_{O1}^{0}$ computed at GGA-PBE level of theory with coupled ARTn/QE on 216-atom slab. Upper panel shows diffusion pathway with selected atomic configurations. Both +2 charged and neutral vacancy pathways are similar and only one is illustrated here. Diffusion begins with a single bond dissociation of O_{3c} atom, creating an undercoordinated surface Ti ion (Ti_{4c}). Displacement of Ti_{4c} ion vertically opens up the passage to downward migration of the surface-bridging oxygen. This oxygen eventually forms sub-bridging oxygen immediately below the topmost surface vacancy. The vacancy migrates through an intermediate unstable state V_{O4}; hence, a characteristic two-step diffusion mechanism is observed. Potential-energy profile of the +2 charged vacancy is on the left, and that for neutral vacancy on the right. Two oxygen atoms that undergo large displacement are black, Ti light blue, the oxygen red, and oxygen vacancy yellow.

TABLE III. Diffusion barriers (E^A) of neutral and $+2$ charged defects on selected surface and subsurface sites of an anatase (101) slab of 216 atoms calculated at the GGA-PBE level using ARTn coupled to QE.

Pathway	E^A neutral vacancy direct pathway (eV)	E^A neutral vacancy inverse pathway (eV)	E^A + 2 charged vacancy direct pathway (eV)	E^A + 2 charged vacancy inverse pathway (eV)
$V_{O1} \rightarrow V_{O5}$	0.52	0.81	0.82	1.01
$V_{O1} \rightarrow V_{O3}$	1.14	0.78	1.15	0.73
$V_{O3} \rightarrow V_{O5}$	0.67	1.33	0.73	1.34
$V_{O5} \rightarrow V_{O6}$	0.40	0.27	0.38	0.19

occurs from V_{O3}^0 to V_{O1}^0 as the first step, and then V_{O1}^0 metastable vacancy diffuses to V_{O5}^0 subsurface site. V_{O3}^0 to V_{O5}^0 pathway is also possible due to lower activation barrier than V_{O3}^0 to V_{O1}^0 pathway. Surface vacancy V_{O3}^{+2} with $+2$ charged state has equal probability to diffuse either to metastable V_{O1}^{+2} site or directly diffuses to V_{O5}^{+2} as these competing migration paths have identical 0.73-eV activation energy barrier. Therefore, a low barrier path of V_{O3}^{+2} to V_{O5}^{+2} is favorable for $+2$ charged vacancy surface-to-subsurface diffusion. However, V_{O1}^{+2} also diffuses to the subsurface overcoming 0.82-eV barrier so that both surface vacancy types eventually migrate to the subsurface. Considering more accurate diffusion directions obtained from 216-atom slab calculation, we conclude that the experimental diffusion range is a result of both

different charges on the vacancies and competing mechanisms on the anatase (101) surface.

B. Bulk and subsurface diffusion pathways

With a clear understanding of surface-to-subsurface diffusion, we now turn to diffusion pathways between bulk and subsurface layer. The diffusion barrier of bulk vacancy migration toward (101) surface calculated using 216-atom surface slab is largely missing in the literature. Our computed bulk vacancy formation energy on the 216-atom slab for the neutral vacancy is larger than the subsurface vacancy formation energy, but smaller than that of the topmost surface vacancy. This is in agreement with Li and co-workers' reported stability order of vacancy formation energies on anatase (101) surface slab [25]. The $+2$ charged bulk vacancy, however, is quantitatively similar in value to the topmost surface vacancy formation energy. The Hubbard model provides higher vacancy formation energies for the bulk than for the subsurface and the topmost surface for neutral and $+2$ charged vacancies (see Fig. S4(b) in Supplemental Material [34]). Therefore, these computed bulk vacancy formation energies indicate bulk-to-subsurface vacancy diffusion in anatase. The *ab initio*-ARTn computed diffusion barriers for the neutral and the $+2$ charged vacancies are tabulated in Table III and potential-energy profiles with the diffusion pathway are illustrated in Fig. 3. The characteristic two-step mechanism through unstable intermediate vacancy site can be observed for bulk-to-subsurface vacancy migration as well. Activation energy barrier for the $+2$ charged vacancy migration from the
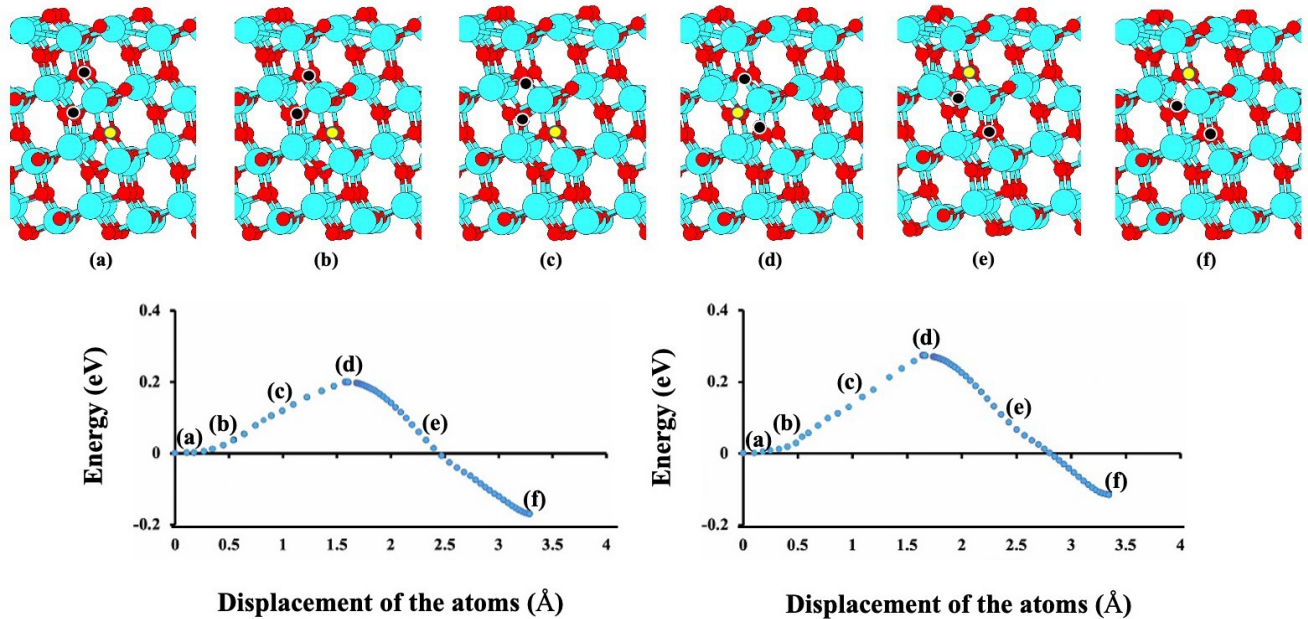

FIG. 3. Potential-energy profile along $V_{O6}^{+2}/V_{O6}^0 \rightarrow V_{O5}^{+2}/V_{O5}^0$ computed at GGA-PBE level of theory with coupled ARTn/QE on 216-atom slab. Upper panel shows diffusion pathway with selected atomic configurations. Both $+2$ charged and neutral vacancy pathways are similar and only one is illustrated here. Surrounding atoms are removed for better visualization of the diffusion pathway. Diffusion begins with a single bond dissociation of O_{3c} atoms indicated in black color. These oxygen atoms significantly displaced during the vacancy migration. The vacancy migrates through an intermediate unstable state; hence, characteristic two-step diffusion mechanism is observed. Potential-energy profile of the $+2$ charged vacancy is on the left, and that for neutral vacancy on the right. The two oxygen atoms that undergo large displacement are black, Ti light blue, the oxygen red, and oxygen vacancy yellow.

TABLE IV. GGA-PBE level computed Ti-Ti ions distance and Ti–O bonds on the 216-atom nondefective slab and defective 215-atom surface slabs with single neutral vacancy are tabulated. Neutral vacancy is used as representative case as both +2 charged and the neutral vacancies show similar diffusion directions on the 216-atom slab. Numbering scheme of the atoms can be found in Fig. S2 in Supplemental Material. O_1, O_5, and O_8 oxygen atoms are deleted to create V_{O1}^0, V_{O5}^0, and V_{O6}^0 vacancies, respectively.

Bonds/ Distance	Nondefective 216 atoms	V_{O1}^0 defective 215 atoms	V_{O5}^0 defective 215 atoms	V_{O6}^0 defective 215 atoms
$Ti_1 - Ti_2$	2.87	3.46	2.85	2.89
$Ti_3 - Ti_4$	2.99	3.17	3.50	2.99
$Ti_5 - Ti_6$	3.05	3.13	3.18	3.49
$Ti_1 - O_1$	1.84	–	1.88	1.84
$Ti_2 - O_1$	1.86	–	1.79	1.83
$Ti_3 - O_5$	1.96	2.10	–	2.11
$Ti_4 - O_5$	1.94	2.05	–	1.77
$Ti_5 - O_8$	2.00	2.05	2.06	–
$Ti_6 - O_8$	1.93	1.99	2.02	–

bulk to the subsurface is 0.19 eV, whereas neutral vacancy migration has to overcome 0.27-eV barrier. Therefore, we unambiguously provide evidence for bulk-to-subsurface diffusion. It is interesting to see that the inverse activation energy barriers for subsurface-to-bulk oxygen vacancy migration are comparatively low as well. This implies that at experimental annealing temperatures, reverse diffusion is also possible. Consequently, dynamic oxygen vacancy migration from bulk to subsurface and subsurface to bulk can be observed. Our results provide theoretical evidence for surface-to-subsurface and bulk-to-subsurface oxygen vacancy diffusion; hence, experimentally observed accumulation of oxygen vacancies at the subsurface is well substantiated [47]. As can be seen, ubiquitous diffusion direction in anatase is bulk-to-subsurface vacancy migration. This is expected as a significant amount of energy is required to create a point defect in highly crystalline nature of the bulk anatase. Therefore, a single vacancy created in the bulk diffuses towards the (101) surface direction to lower the energy of the structure.

However, surface-to-subsurface vacancy diffusion is not quite intuitive. Thus, we tabulate Ti–Ti and Ti–O bond distances of the defect-free and defective anatase (101) surfaces with single neutral vacancy on 216-atom slab in Table IV. The topmost surface $Ti_1 - Ti_2$ distance, $Ti_1 - O_1$ and $Ti_2 - O_1$ bond lengths are shorter than the second ($Ti_3 - Ti_4$, $Ti_3 - O_5$, and $Ti_4 - O_5$) and third layers ($Ti_5 - Ti_6$, $Ti_5 - O_8$, and $Ti_6 - O_8$) in defect-free structure. Also, the topmost surface maintains shorter bond lengths and distance between Ti ions in the presence of the subsurface V_{O5}^0 and the bulk V_{O6}^0 vacancies. Moreover, the $Ti_1 - Ti_2$ distance expands ~0.6 Å in order to accommodate V_{O1}^0 vacancy, which is the largest among three vacancies compared in Table IV. These observations indicate the anatase (101) surface topmost layer is compressively strain. Thus, to accommodate topmost surface vacancy requires substantial amount of energy to distort the surface structure. As a consequence, topmost surface vacancy is metastable and diffuses to the subsurface. Although it is difficult to find such a distinctive structural trend to support

bulk-to-subsurface diffusion, substantially similar bond distances ($Ti_3 - O_5$ and $Ti_4 - O_5$) in the defect-free structure suggest the second layer is minimally strain on the anatase (101) surface. This results in a lower vacancy formation energy on the subsurface than the bulk. An oxygen-atom removal from the subsurface and the bulk create stable fivefold Ti ions in both cases do not explain extra stability on subsurface; however, strain on different surface layers provides more consistent explanation. Furthermore, higher stability of the +2 charged topmost surface on 72-atom surface slab provides plausibility to stabilize topmost surface due to vertical displacement of Ti_{4c}^{+4} ion neighboring the vacancy. In fact, single titanium ion displaced towards the vacuum at the adsorption site can be observed in recent computational studies of H_2O and H_2S, which are claimed to induce subsurface-to-surface vacancy diffusions [22,23]. This also suggests charge vacancy site on the anatase (101) surface may be reconstructed in such way that the surface can engineer to reverse the natural diffusion direction. Therefore, +2 charged vacancy diffusion is equally important to understand surface reactivity and to design surface-engineered structures of TiO_2-based photocatalysts.

IV. CONCLUSIONS

We apply the activation-relaxation technique nouveau coupled with the QUANTUM ESPRESSO package to predict the +2 charged and the neutral vacancies diffusion barriers on the anatase (101) surface. Five inequivalent oxygen vacancy sites are selected to understand the surface and subsurface vacancy diffusion. For initial studies, the 72-atom anatase (101) surface slab is used. This small-slab model stabilizes the topmost surface +2 charged vacancy due to surface reconstruction; hence, subsurface-to-surface vacancy diffusion is observed. This is attributed to the small cell that is unable to accommodate the strong Coulomb repulsion between Ti^{+4} ions and +2 charged vacancy. With sufficient surface relaxation, a larger 216-atom slab model shows rather that both +2 charged and neutral vacancies diffusion in the same the top surface layer to the subsurface direction. The diffusion barriers for the +2 charged oxygen vacancy migration are 0.82 eV for direct diffusion, and 1.01 eV for inverse diffusion. The neutral oxygen vacancy diffusion shows a lower barrier for the direct diffusion to the subsurface, i.e., 0.52 eV, and 0.81-eV inverse barrier for the surface migration. In addition, V_{O3}^{+2}/V_{O3}^0 surface vacancies can migrate toward the subsurface with competing diffusion mechanisms. In fact, V_{O3}^{+2} to V_{O5}^{+2} diffusion has a 0.73-eV barrier, which is smaller than the V_{O1}^{+2} to V_{O5}^{+2} activation barrier. As consequences of vacancy-charged and competing diffusion mechanisms, a range of diffusion barriers for surface-to-subsurface oxygen vacancy migration on the anatase (101) surface is observed. Moreover, we investigate the bulk oxygen vacancy formation energies for both intrinsic vacancy types and their diffusion barriers. Bulk vacancies are less stable than the subsurface vacancies. The activation energy barrier for the +2 charged vacancy migration from the bulk to the subsurface is 0.19 eV, whereas neutral vacancy migration has to overcome the 0.27-eV barrier. Therefore, we unambiguously provide evidence for bulk-to-subsurface diffusion. Inverse barriers for bulk-to-subsurface

diffusion suggest dynamic diffusion from bulk to subsurface and subsurface to bulk. Our results provide theoretical evidence for surface-to-subsurface and bulk-to-subsurface oxygen vacancy diffusion, and hence the experimentally observed accumulation of oxygen vacancies at the subsurface is well substantiated. Although our small-surface slab stabilizes $+2$ charged vacancy on the topmost surface as opposed to more reliable larger slab model, it provides information that might be useful to stabilize topmost surface oxygen vacancy. The topmost vacancy stability due to vertical displacement of Ti_{4c}^{+4} ion neighboring the vacancy can be used to reverse the natural diffusion direction on the anatase (101) surface. Therefore, we suggest that such a surface reconstruction may be the origin of the reversibility of the diffusion direction from the subsurface to the surface. In addition, semilocal approximation and the Hubbard model computed vacancy formation energies and the diffusion barriers indicate that semilocal approximation is good enough to investigate diffusion barriers. Moreover, this study provides an in-depth understanding of the diffusion of intrinsic oxygen vacancies on the surface of the anatase (101) using the GGA-PBE and the DFT+U levels of theories, as well as the diffusion barriers and diffusion paths for all inequivalent surface oxygen vacancy sites and the bulk, which are largely lacking in the literature. In addition, $+2$ charged and neutral vacancy diffusion is addressed in detail. More widely, this investigation sheds light also on the intricacies of modeling charged oxygen vacancy migration on the anatase (101) surface. Furthermore, this paper may serve the experimental community in devising methods to engineer the (101) surface of anatase to acquire desired surface reactions by tuning the direction of diffusion through surface reconstruction.

[1] N. Serpone, J. Phys. Chem. B **110**, 24287 (2006).

[2] M. E. Simonsen, H. Jensen, Z. Li, and E. G. Søgaard, J. Photochem. Photobiol. A **200**, 192 (2008).

[3] Y. Hu and C. Yuan, J. Cryst. Growth **274**, 563 (2005).

[4] E. Baldini, L. Chiodo, A. Dominguez, M. Palummo, S. Morser, M. Y. Rizi, G. Auboeck, B. P. P. Mallett, H. Berger, A. Magrez *et al.*, Nat. Commun. **8**, 13 (2017).

[5] R. F. Howe and M. Gratzel, J. Phys. Chem. **91**, 3906 (1987).

[6] J. R. De Lile, S. G. Kang, Y.-A. Son, and S. G. Lee, ACS omega **4**, 8056 (2019).

[7] M. Sahoo, A. Yadav, S. Jha, D. Bhattacharyya, T. Mathews, N. Sahoo, S. Dash, and A. Tyagi, J. Phys. Chem. C **119**, 17640 (2015).

[8] R. Asahi, T. Morikawa, T. Ohwaki, K. Aoki, and Y. Taga, Science **293**, 269 (2001).

[9] V. N. Kuznetsov and N. Serpone, J. Phys. Chem. B **110**, 25203 (2006).

[10] C. Foo, Y. Li, K. Lebedev, T. Chen, S. Day, C. Tang, and S. C. E. Tsang, Nat. Commun. **12**, 661 (2021).

[11] T. Ihara, M. Miyoshi, M. Ando, S. Sugihara, and Y. Iriyama, J. Mater. Sci. **36**, 4201 (2001).

[12] K. Qi, R. Selvaraj, T. Al Fahdi, S. Al-Kindy, Y. Kim, G.-C. Wang, C.-W. Tai, and M. Sillanpää, Appl. Surf. Sci. **387**, 750 (2016).

[13] A. Lisachenko, V. Kuznetsov, M. Zakharov, and R. Mikhailov, Kinet. Catal. **45**, 189 (2004).

[14] A. G. Thomas, W. R. Flavell, A. R. Kumarasinghe, A. K. Mallick, D. Tsoutsou, G. C. Smith, R. Stockbauer, S. Patel, M. Gräetzel, and R. Hengerer, Phys. Rev. B **67**, 035110 (2003).

[15] A. Janotti, J. B. Varley, P. Rinke, N. Umezawa, G. Kresse, and C. G. Van de Walle, Phys. Rev. B **81**, 085212 (2010).

[16] C. Spreafico and J. VandeVondele, Phys. Chem. Chem. Phys. **16**, 26144 (2014).

[17] P. Scheiber, M. Fidler, O. Dulub, M. Schmid, U. Diebold, W. Hou, U. Aschauer, and A. Selloni, Phys. Rev. Lett. **109**, 136103 (2012).

[18] B. J. Morgan and G. W. Watson, J. Phys. Chem. C **114**, 2321 (2010).

[19] H. Cheng and A. Selloni, Phys. Rev. B **79**, 092101 (2009).

[20] H. Cheng and A. Selloni, J. Chem. Phys. **131**, 054703 (2009).

[21] M. Setvín, U. Aschauer, P. Scheiber, Y.-F. Li, W. Hou, M. Schmid, A. Selloni, and U. Diebold, Science **341**, 988 (2013).

[22] Y. Li and Y. Gao, Phys. Rev. Lett. **112**, 206101 (2014).

[23] Z.-W. Wang, W.-G. Chen, D. Teng, J. Zhang, A.-M. Li, Z.-H. Li, and Y.-N. Tang, J. Phys. Chem. C **126**, 3939 (2022).

[24] P. Deák, J. Kullgren, and T. Frauenheim, Phys. Status Solidi (RRL) **8**, 583 (2014).

[25] H. Li, Y. Guo, and J. Robertson, J. Phys. Chem. C **119**, 18160 (2015).

[26] A. Jay, C. Huet, N. Salles, M. Gunde, L. M. Samo, N. Richard, G. Landa, V. Goiffon, S. De Gironcoli, A. Hemeryck *et al.*, J. Chem. Theory Comput. **16**, 6726 (2020).

[27] P. Giannozzi, S. BAroni, N. Bonini, M. Calandra, R. Car, C. Cavazzoni, D. Cereoli, G. L. Chiarotti, M. Cococcioni, I. Dabao *et al.*, J. Phys.: Condens. Matter **21**, 395502 (2009).

[28] P. Giannozzi, O. Andreussi, T. Brumme, O. Bunau, M. B. Nardeli, M. Calandra, R. Car, C. Cavazzoni, C. Ceresoli, M. Cococcioni *et al.*, J. Phys.: Condens. Matter **29**, 465901 (2017).

[29] D. Vanderbilt, Phys. Rev. B **41**, 7892 (1990).

[30] J. K. Burdett, T. Hughbanks, G. J. Miller, J. W. Richardson Jr, and J. V. Smith, J. Am. Chem. Soc. **109**, 3639 (1987).

[31] J. P. Perdew, K. Burke, and M. Ernzerhof, Phys. Rev. Lett. **77**, 3865 (1996).

[32] V. I. Anisimov, F. Aryasetiawan, and A. Lichtenstein, J. Phys.: Condens. Matter **9**, 767 (1997).

[33] M. Cococcioni and S. de Gironcoli, Phys. Rev. B **71**, 035105 (2005).

[34] See Supplemental Material at http://link.aps.org/supplemental/10.1103/PhysRevMaterials.7.034602 for DFT+U results, comparison of neutral and 2+ charged vacancy formation energies, PDOS diagrams, and all the diffusion pathways.

[35] J. D. Head and M. C. Zerner, Chem. Phys. Lett. **122**, 264 (1985).

[36] F. Bruneval, J.-P. Crocombette, X. Gonze, B. Dorado, M. Torrent, and F. Jollet, Phys. Rev. B **89**, 045116 (2014).

[37] R. Malek and N. Mousseau, Phys. Rev. E **62**, 7723 (2000).

[38] N. Mousseau and G. T. Barkema, Phys. Rev. E **57**, 2419 (1998).

[39] G. Barkema and N. Mousseau, Phys. Rev. Lett. **77**, 4358 (1996).

[40] H. D. Simon, Math. Comput. **42**, 115 (1984).

[41] J. P. W. Treacy, H. Husain, X. Torrelles, D. C. Grinter, G. Cabailh, O. Bikondoa, C. Nicklin, S. Selcuk, A. Selloni, R. Lindsay, and G. Thornton, Phys. Rev. B **95**, 075416 (2017).

[42] Y. Zhang, F. Hao, C. Liu, and X. Chen, Theor. Chem. Acc. **135**, 1 (2016).

[43] A. Raghav, A. T. Hanindriyo, K. Utimula, M. Abbasnejad, R. Maezono, and E. Panda, Comput. Mater. Sci. **184**, 109925 (2020).

[44] M. H. Naik and M. Jain, Comput. Phys. Commun. **226**, 114 (2018).

[45] J. Xiao, K. Yang, D. Guo, T. Shen, H.-X. Deng, S.-S. Li, J.-W. Luo, and S.-H. Wei, Phys. Rev. B **101**, 165306 (2020).

[46] M. F. Tabriz, B. Aradi, T. Frauenheim, and P. Deák, Comput. Phys. Commun. **240**, 101 (2019).

[47] Y. He, O. Dulub, H. Cheng, A. Selloni, and U. Diebold, Phys. Rev. Lett. **102**, 106105 (2009).